

Mixed Attention with Deep Supervision for Delineation of COVID Infection in Lung CT

Pallabi Dutta*, Sushmita Mitra

*Machine Intelligence Unit, Indian Statistical Institute, Kolkata 700108, India.
Email: duttapallabi2907@gmail.com, sushmita@isical.ac.in*

Abstract

The COVID-19 pandemic, with its multiple variants, has placed immense pressure on the global healthcare system. An early effective screening and grading become imperative towards optimizing the limited available resources of the medical facilities. Computed tomography (CT) provides a significant non-invasive screening mechanism for COVID-19 infection. An automated segmentation of the infected volumes in lung CT is expected to significantly aid in the diagnosis and care of patients. However, an accurate demarcation of lesions remains problematic due to their irregular structure and location(s) within the lung.

A novel deep learning architecture, Mixed Attention Deeply Supervised Network (*MiADS-Net*), is proposed for delineating the infected regions of the lung from CT images. Incorporating dilated convolutions with varying dilation rates, into a mixed attention framework, allows capture of multi-scale features towards improved segmentation of lesions having different sizes and textures. Mixed attention helps prioritise relevant feature maps to be probed, along with those regions containing crucial information within these maps. Deep supervision facilitates discovery of robust and discriminatory characteristics in the hidden layers at shallower levels, while overcoming the vanishing gradient. This is followed by estimating the severity of the disease, based on the ratio of the area of infected region in each lung with respect to its entire volume. Experimental results, on three publicly available datasets, indicate that the MiADS-Net outperforms several state-of-the-art architectures in the COVID-19 lesion segmentation task; particularly in defining structures involving complex geometries.

Keywords: Segmentation, Mixed attention, Deep supervision, Dilated convolution

1. Introduction

A critical step in the fight against COVID-19 is an effective screening of the level of infection in patients; such that those seriously affected can receive immediate treatment and care, as well as be isolated to mitigate the spread of the virus. The gold standard screening method currently used for detecting COVID-19 cases is the reverse transcription polymerase chain reaction (RT-PCR) testing, which is a very time-consuming, laborious, and complicated manual process. The test is uncomfortable, invasive, uses nasopharyngeal swabs, and has high false negative rates; with outcome being dependent on sampling errors and low viral load. Given that CT is reliable to check changes in the lungs, its importance in the context of COVID-19 becomes all the more evident.

*Corresponding author

Conspicuous ground-glass opacity (GGO) and multiple mottling lesions, in the peripheral and posterior lungs on CT images, are hallmark characteristics of COVID-19 pneumonia [1]. While the GGO are hazy darkened spots in the lung, diffuse enough such that they do not block underlying blood vessels or lung structures, the consolidations correspond to areas of increased lung density [1]. It is observed that with time these infection characteristics became more frequent, and are likely to spread across both lungs. Morozov *et al.* [2] suggested a partially quantitative severity grading system on a scale of 0 to 4, with a step value of 25%, based on the percentage of the diseased lung tissue. While CT-0 represents healthy cohorts, grade CT-4 refers to those patients with affected lung regions > 75%. This scale was assigned by experts based on visual inspection of the lung CT scans of infected patients.

In order to speed up the discovery of disease mechanisms, machine learning and deep learning [3] can be effectively employed to detect abnormalities and extract textural features of the altered lung parenchyma; to be subsequently related to specific signatures of the COVID-19 virus. Automated segmentation of the lung region and lesion from CT can help outline the volume of interest (VOI) for a fast detection and grading of the severity of infection. A consistent and reproducible method, for the rapid evaluation of high volumes of screening or diagnostic thoracic CT studies, is possible with artificial intelligence. Demarcation of affected lung tissues in the CT slices demands high precision. Deep learning enables circumventing the visual approximation by radiologists, to produce accurate decisions; particularly in the scenario of high volumes of disease cases.

Typically deep learning requires a machine to learn automatically from raw data to discover representations needed for detection or classification. In the context of medical images, it directly uses pixel values of the images at the input; thereby, overcoming the manual errors caused by inaccurate segmentation and/or subsequent hand-crafted feature extraction. Convolution neural networks (CNNs) [3] constitute one of the popular models of deep learning. Some of the commonly used deep learning models in medical applications include CNN, ResNet [4], Res2Net [5], DenseNet [6], and SegNet [7].

Custom architectures, like the *U-Net* [8], have been designed for segmentation with promising results. Here the skip connections between the symmetric down-sampling (encoder) and up-sampling (decoder) paths, in the fully convolutional framework, provide local (high resolution) information in the global context during up-sampling; thereby, resulting in improved localization of the target region with more precise segmentation results. However, it is observed that the target lesion regions (like GGO) in lung CT scans of COVID-19 patients are of lower contrast with blurred edges, particularly in the early stages. They also appear in varying shapes and sizes within the lung. Attention modules were incorporated in the vanilla *U-Net* framework [9], in order to enhance its segmentation performance. The encoder feature maps were recalibrated spatially with the aid of decoder feature maps. The attention module thus helped the network to focus only on the relevant regions of interest in the target, while suppressing the contribution from irrelevant areas.

Both ResNet and Res2Net incorporate residual connections, to help combat the vanishing gradient issue, while developing deeper networks. Res2Net additionally employs parallel cascading convolution operations within a block. This helps capture multi-scale features in the input volume. The DenseNet makes use of residual connections by bridging all convolution layers with each other. It additionally promotes re-use of feature maps, with further improvement in performance. The *U-Net++* [10] and Residual *U-Net* [11] are also used in medical image segmentation. The *U-Net++* inserts multiple convolution blocks between the encoding and decoding pathway of its *U-Net*

backbone. This helps narrow down the semantic gap between the activation maps produced by the encoders and decoders; thereby, reducing the complexity of optimization. An exhaustive survey on the role of artificial intelligence in analysing and predicting COVID-19 can be found in Ref. [12, 13].

A novel Mixed Attention Deeply Supervised Network (*MiADS-Net*) is developed for accurately demarcating the COVID-19 infection in lung CT images. It is capable of learning generalized representations of the irregularly structured infected regions. The contribution of this research is summarized below.

- The classic symmetric encoder-decoder path of the *U-Net* is enriched with a mixed attention mechanism, that helps highlight “which” activation maps are of higher relevance along with “where” to look for the necessary characteristic features in these maps.
 - Channel attention is responsible for highlighting relevant maps in the input set. Incorporation of depth-wise and dilated convolutions helps generate the relevant recalibrating weights from the semantically rich decoder activation maps.
 - Locations of interest within the accentuated maps are further emphasized by assigning higher weights to relevant locations, while down-weighting the remaining “less relevant” regions; with the weights being derived from the set of decoder activation maps.
- Deep supervision is incorporated by attaching additional decoder branches to *shallower* levels of the encoder during segmentation. This helps learn robust representations at earlier levels of the architecture, while avoiding occurrence of vanishing gradients.
- A novel linear combination of Dice Loss and Focal Tversky Loss is used to handle the issue of class imbalance, while simultaneously minimizing the occurrence of False Positives and False Negatives in the output.

The rest of the paper is organized as follows. Section 2 briefly describes state-of-the-art literature on the use of deep learning for segmentation of COVID lesions from lung CT images. In Section 3 we introduce the proposed *MiADS-Net*. Experimental results are discussed in Section 4. Comparative study is provided with state-of-the-art models, including the *U-Net* [8] and its variants like *U-Net++* [10], Residual *U-Net* [11], and Attention *U-Net* [9], on segmentation of the lesions. The demarcated region is used to compute the percentage of infection in the lung; on the basis of which a grading of the severity of the disease is evaluated. The superiority of the *MiADS-Net* is demonstrated on CT slices extracted from four sets of publicly available data, *viz.* MOSMED [14], MedSeg-COV-1 [15], MedSeg-COV-2 [16], and COV-CT-Lung-Inf-Seg [17]. Finally Section 5 concludes the article.

2. Deep Learning for Delineating COVID-Infected CT Lesions

A retrospective, multi-centric study [18] employed the ResNet-50, with *U-Net* for segmenting the lung region from CT, to differentiate between COVID-19 viral pneumonia, Community acquired pneumonia (CAP) and other non-pneumonia images. The datasets were collected from six hospitals between August 2016 and February 2020, and consisted of 4356 chest CT examinations from 3,322 patients. Similarly, a 3D DenseNet was trained in a diverse multinational cohort of 1280 patients [19] to localize parietal pleura/ lung parenchyma, followed by classification of

COVID-19 pneumonia; with high sensitivity and specificity on an independent test set of 1337 patients. Visualization of activation regions was performed using Grad-CAM to assess association of peripheral regions of the lung across variable amounts of disease burden. A novel Joint Classification and Segmentation system was designed [20] to perform real-time and explainable diagnosis based on 1,44,167 CT images of 400 COVID-19 patients and 350 uninfected cases. Of these, 3,855 images of 200 patients were annotated with fine-grained pixel-level labels, lesion counts, infected areas and locations, benefiting various diagnosis aspects. With the explainable classification outputs coming from Res2Net, and the corresponding fine-grained lesion segmentation resulting from VGG-16, the system helped simplify and accelerate the diagnostic process for radiologists.

An attention-based deep 3D multiple instance learning (AD3D-MIL) was developed [21] for the effective screening of COVID-19. A patient-level label was assigned to each 3D chest CT, which was viewed as a bag of instances. An attention-based pooling approach to 3D instances provided insight into the contribution of each instance towards the bag label. The model was evaluated on a multi-center collection of 460 chest CT samples, encompassing 230 CT slices from 79 patients with COVID-19, 100 CT slices from 100 patients with common pneumonia, and 130 CT slices from 130 people without any kind of pneumonia. A series of empirical studies demonstrated an overall accuracy of 97.9%, Area Under Curve (*AUC*) of 99.0%, and Cohen Kappa score of 95.7%, along with enhanced generalization and interpretability.

The segmentation performance of the *U*-Net and SegNet was compared [22] on one out of the two datasets in MedSeg-29 [16], obtained from the Italian Society of Medical Interventional Radiology. It is a cohort of 100 single slice axial CT scans from more than 40 patients. While binary segmentation identified the lung tissues infected by COVID-19 virus, the multi-class segmentation delineated the different lesion pathologies. Here 72 slices were considered in the training set, 10 slices in the validation set, and 18 slices for the test set. In case of binary segmentation, both the models attained a Dice Score Coefficient (*DSC*) $> 70\%$, with the SegNet outperforming the *U*-Net by around 1% value. However, both exhibited poor performance in multi-class segmentation, particularly for identifying the pleural effusions, possibly due to scarcity of corresponding CT slices.

A multi-task architecture was introduced [23] to simultaneously perform classification and segmentation. The lung CT scans were grouped into COVID-19 infected and non-infected categories, while also ranking the infected scans in decreasing order of severity. The infected regions were first segmented to calculate the ratio of the affected lung region w.r.t. the total lung region, over each slice. The maximum value was used to compute the severity stage, as per the guidelines of the Fleischner Society. A basic 2D *U*-Net was first trained on *NSCLC-Radiomics* and *LUNA16*, for the lung region segmentation. The classification into COVID-19 infected and non-infected samples was performed with training on the MOSMED and NSCLC Radiomics datasets. The segmentation module was trained on MedSeg-29 and 50 annotated scans from MOSMED-1110. The *AUC* score for the classification task was around 0.90, with *DSC* value for segmentation being 0.61 ± 0.02 .

The DUDA-Net [24] employed a cascaded pair of *U*-Nets, with the first one extracting the lung region from the CT slice to make it easier for subsequent focus on the COVID-19 lesions. Attention modules with dilated convolutions helped the second *U*-Net to effectively capture multi-scale information, and re-weight relevant channels of the input feature map volume for better focus on the region of interest. This strategy helped decrease any segmentation error caused by smaller-sized lesions. However this entailed an increase in computational complexity

in terms of the parameters involved. The dataset used was Coronacases [17]. The role of different loss functions were investigated. Since most of the slices did not contain lesions, only 557 CT slices were extracted to prevent class imbalance. The model resulted in a DSC of 87.06%, sensitivity (SEN) of 90.85%, specificity (SPE) of 99.59%, and AUC of 0.965.

A pair of attention modules were introduced [25] in the U -Net framework, to enhance feature map volumes along the skip connections as well as the up-sampled feature maps of the decoder. This dual attention strategy helped re-weight the feature maps, both spatially and channel-wise, for improved segmentation of the infected lung tissues in the slices. The dilated convolutions helped generate larger receptive fields. Experimental results were provided on the MedSeg-29, and the Coronacases [17] from Radiopedia. The model achieved a DSC of 0.7047, along with a recall score of 0.6626 and a pixel error value of 0.0323.

Use of simultaneous channel-wise and spatial attention in the vanilla U -Net framework, along with residual attention blocks, helped capture multi-scale contextual relationships by stacking multiple dilated convolutions of varying dilation rates [26]. Additional deep supervision was employed by concatenating the up-sampled decoder maps. The CT scans were taken from both datasets of MedSeg-29. The authors reported $DSC > 80\%$; thereby, corroborating the need for both spatial and channel-wise attention for better feature representation, resulting in enhanced performance. The focal Tversky loss was used to effectively segment smaller lesions.

The nCoVSegNet [27] employed two-stage transfer learning to deal with data scarcity in large annotated COVID-19 datasets. It acquired knowledge both from the ImageNet [28] and a lung nodule detection dataset (LIDC-IDRI), to delineate COVID-19 lesions from lung CT scans in the MOSMED dataset. A global context-aware module, employing convolution blocks of varying sizes, helped capture multi-scale features. A Dual-Attention fusion module, incorporating both channel and spatial attention, enabled improved segmentation performance. Authors reported a DSC of 0.6894 on Coronacases dataset, and 0.6843 on the MOSMED dataset.

The Inf-Net [29] involved a parallel partial decoder to aggregate high-level features for generating a global segmentation map. A reverse attention mechanism, with an additional edge attention module, was incorporated for better delineation of the blurred edges of the lesions. The semi-supervised framework, requiring only a few labeled images and leveraging primarily unlabeled data, helped improve the learning ability with a higher performance. A DSC of 0.682 was reported on the MedSeg-29.

A lightweight CNN model LCOV-Net [30] employed a separable convolution operation, in lieu of the conventional convolution block, to capture features from 3D lung CT volumes; thereby, significantly reducing the model parameters to make it computationally lighter with faster training time. Attention mechanism was incorporated to recalibrate the feature maps, in order to emphasize the relevant features w.r.t. the region of interest. The authors acquired lung CT scans of 130 COVID-19 patients from 10 different hospitals in their research, with a reported DSC of 78.67 ± 13.11 .

3. Mixed Attention Deeply Supervised Network (*MiADS-Net*)

This section describes the *MiADS-Net* along with its primary components, *viz.* mixed attention [through *Spatial-Channel (SpaCh)* block] and the deep supervision mechanism. The loss function employed is also outlined, along with the performance evaluation metrics used.

3.1. Architecture

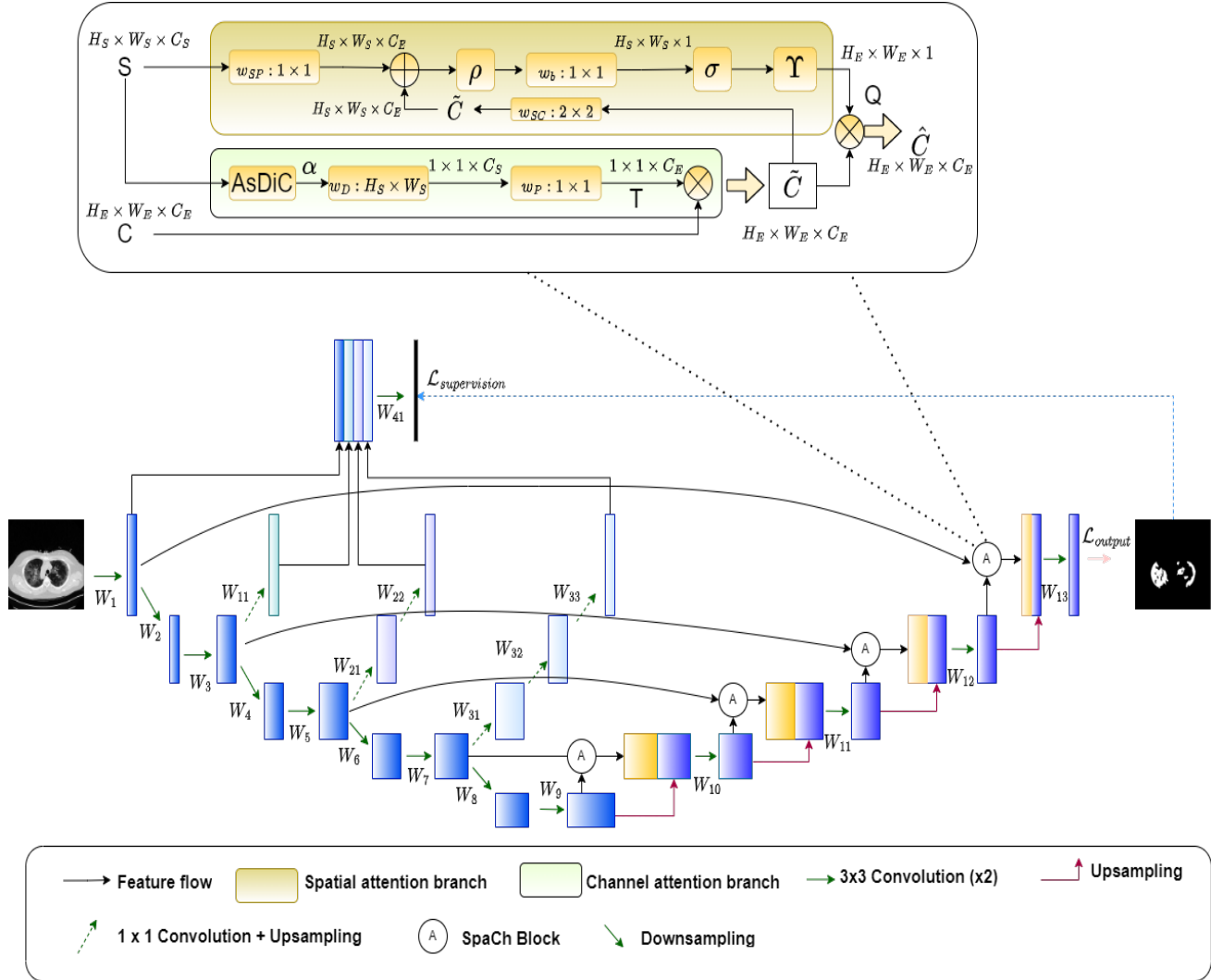


Figure 1: The *MiADS-Net*, with an enlarged view of the *SpaCh* block on top

The *MiADS-Net* of Fig. 1 is built on the basic *U-Net* backbone. The CT slices are provided as input to a five level encoder-decoder network, where level l consists of two convolution blocks with 64×2^l filters each. A down-sampling convolution block reduces the spatial dimensions of the feature maps to half, as the feature volume percolates from one encoder level to the next. We prefer the convolution operation, instead of max pooling, as the latter may induce information loss in certain circumstances; particularly, when the target region is not visually salient. The appearance of COVID-19 lesions like GGO's, having blurred edges and poor contrast, often pose such a problem. The skip connections for concatenating the output feature map volume at level l of the encoder and the input volume at the corresponding level of the decoder get enriched with a mixed attention mechanism, called *Spatial-Channel (SpaCh)* attention module. It helps highlight relevant maps, along with important locations within them, before concatenation. Additional up-sampling paths are introduced at the second, third and fourth levels of the encoder arm for deep supervision. These aid the maps at shallower levels to learn more meaningful features, while overcoming the vanishing gradient problem. Sigmoid activation is applied to the feature map at the end of the

Level	Encoder		Decoder		Deep Supervision	
	Filters	Output	Filters	Output	Filters	Output
1	Input Layer	$512 \times 512 \times 1$	UP2D	$512 \times 512 \times 128$	Conv2D+GN+UP2D	$512 \times 512 \times 64$
	Conv2D+ZP	$512 \times 512 \times 64$	Conv2D+ZP	$512 \times 512 \times 64$		
	GN	$512 \times 512 \times 64$	GN	$512 \times 512 \times 64$		
	Conv2D+ZP	$512 \times 512 \times 64$	Conv2D+ZP	$512 \times 512 \times 64$		
	Conv2D	$256 \times 256 \times 64$	Output Layer	$512 \times 512 \times 1$		
2	Conv2D+ZP	$256 \times 256 \times 128$	UP2D	$256 \times 256 \times 256$	$(\text{Conv2D+GN+UP2D}) \times 2$	$512 \times 512 \times 64$
	GN	$256 \times 256 \times 128$	Conv2D+ZP	$25 \times 256 \times 128$		
	Conv2D+ZP	$256 \times 256 \times 128$	GN	$256 \times 256 \times 128$		
	Conv2D	$128 \times 128 \times 128$	Conv2D+ZP	$256 \times 256 \times 128$		
3	Conv2D+ZP	$128 \times 128 \times 256$	UP2D	$128 \times 128 \times 512$	$(\text{Conv2D+GN+UP2D}) \times 3$	$512 \times 512 \times 64$
	GN	$128 \times 128 \times 256$	Conv2D+ZP	$128 \times 128 \times 256$		
	Conv2D+ZP	$128 \times 128 \times 256$	GN	$128 \times 128 \times 256$		
	Conv2D	$64 \times 64 \times 256$	Conv2D+ZP	$128 \times 128 \times 256$		
4	Conv2D+ZP	$64 \times 64 \times 512$	UP2D	$64 \times 64 \times 1024$	-	
	GN	$64 \times 64 \times 512$	Conv2D+ZP	$64 \times 64 \times 512$		
	Conv2D+ZP	$64 \times 64 \times 512$	GN	$64 \times 64 \times 512$		
	Conv2D	$32 \times 32 \times 512$	Conv2D+ZP	$64 \times 64 \times 512$		
5	Conv2D+ZP	$32 \times 32 \times 1024$	-		-	
	GN	$32 \times 32 \times 1024$				
	Conv2D+ZP	$32 \times 32 \times 1024$				

Table 1: Architectural details of the *MiADS-Net*. Here Conv2D indicates 2D convolution, ZP represents zero padding, GN denotes Group Normalization, and UP2D corresponds to 2D upsampling with bilinear interpolation.

decoder path, to generate the final output depicting the infected region. The MiADS-Net framework is summarized in Table 1.

3.2. Mixed attention

Concatenating encoder activation maps with decoder feature representations, via skip connections, helps incorporate lower-level spatial information towards improved target localization. The attention mechanism allows focus on the relevant activation regions. Mixed attention, employed through the *SpaCh* block to introduce simultaneous channel and spatial attention, enables better segmentation of the target lesions. While channel attention highlights feature maps of interest in the input volume, the spatial attention recalibrates the output to highlight important locations within each such activated map. The *MiADS-Net* employs the spatial and channel attention mechanisms in a sequential manner, instead of applying them independently on the encoder volume to eventually combine the results as in Ref. [26]. Hence the important feature maps are initially highlighted, followed by their relevant locations getting emphasized thereafter. As a result, performance improvement is achieved with an optimization of computational resources.

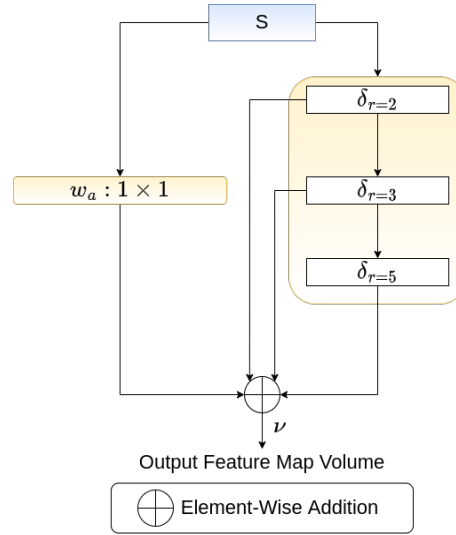


Figure 2: Assembled Dilated Convolution (*AsDiC*) kernels, involving different dilation rates

3.2.1. Channel attention

Consider the lower branch of the *SpaCh* block at the top of Fig. 1. Let $\mathbf{C} = [C^1, C^2, \dots, C^{C_E} | C^i \in \mathbb{R}^{H_E \times W_E}]$ be the input volume from the encoder arm, where C_E indicates the number of encoder channels. Let C_S correspond to the number of decoder channels, $\mathbf{W}_S = [w_S^1, w_S^2, \dots, w_S^{C_S}]$ be the dilated convolution kernels, and $\mathbf{W}_a = [w_a^1, w_a^2, \dots, w_a^{C_S} | w_a^i \in \mathbb{R}^{1 \times 1}]$ refer to the point-wise convolution kernels. The set of semantically rich activation maps $\mathbf{S} = [S^1, S^2, \dots, S^{C_S} | S^i \in \mathbb{R}^{H_S \times W_S}]$ is passed through the *AsDiC* block, involving an assembly of convolutions with varying dilation rates $r = 2, 3, 5$ (as in Fig. 2). The i th dilated convolution δ_r^i for kernel w_S^i and feature map f^j , is expressed as

$$\delta_r^i = \sum_{j=1}^{C_S} \sum_{p=-\frac{(m-1)}{2}}^{\frac{(m+1)}{2}} \sum_{q=-\frac{(n-1)}{2}}^{\frac{(n+1)}{2}} w_S^i(p, q) f^j(a + rp, b + rq). \quad (1)$$

The application of multiple dilated convolutions on \mathbf{S} , in a pipeline of the *AsDiC* block, yields the output feature map volume $\boldsymbol{\nu}$ with component $\nu^i \in \mathbb{R}^{H_S \times W_S}$ indicating the i th activation map. Hence

$$\nu^i = \delta_{r=2}^i(\mathbf{S}; \Omega_{\delta_{r=2}}) \oplus \delta_{r=3}^i\{\delta_{r=2}^i(\mathbf{S}; \Omega_{\delta_{r=2}}); \Omega_{\delta_{r=3}}\} \oplus \delta_{r=5}^i[\delta_{r=3}^i\{\delta_{r=2}^i(\mathbf{S}; \Omega_{\delta_{r=2}}); \Omega_{\delta_{r=3}}\}; \Omega_{\delta_{r=5}}] \oplus \sum_{j=1}^{C_S} w_a^k * S^j. \quad (2)$$

Here $\Omega_{\delta_{r=k}}$ represents the set of parameters (at dilation rate k) defining the dilated convolutions \mathbf{W}_S , with \oplus indicating element-wise addition, w_a^k the k th point-wise convolution filter and S^j being the j th activation map in \mathbf{S} . Use of multiple dilated convolutions, with varying dilation rates, produces multi-scalar views from the semantically rich activation map volume at deeper levels of MiADS-Net. This helps capture the appropriate characteristics of the target COVID-19 lesions, which inherently exhibit inconsistent shapes and sizes. Use of point-wise convolution, along with multiple stacked dilated convolutions, help retain information from the regions overlooked by dilated convolutions. Larger field of view, without greater convolution kernel parameters, reduces the computational cost.

Let us now focus on the lower branch of the *SpaCh* block in Fig. 1. Depth-wise convolutions are applied to the output volume $\boldsymbol{\nu} = [\nu^1, \nu^2, \dots, \nu^{C_S} | \nu^i \in \mathbb{R}^{H_S \times W_S}]$ of *AsDiC* to squeeze its dimensions to $1 \times 1 \times C_S$, followed by

a point-wise convolution for further dimensionality reduction in order to match the number of channels C_E of the encoder feature maps \mathbf{C} . It also introduces non-linearity to help learn more complex patterns. This is formulated as

$$\Delta^i = w_D^i * \nu^i, \quad (3)$$

where $\mathbf{W}_D = [w_D^1, w_D^2, \dots, w_D^{C_E} | w_D^i \in \mathbb{R}^{H_S \times W_S}]$ represent the depth-wise convolution kernels, and $\Delta^i \in \mathbb{R}^{1 \times 1}$ is the resultant i th output map. The derived weights $T^i \in [0, 1]$ are computed as

$$T^i = \sum_{j=1}^{C_S} w_P^k * \Delta^j, \quad (4)$$

where $\mathbf{W}_P = [w_P^1, w_P^2, \dots, w_P^{C_S} | w_P^i \in \mathbb{R}^{1 \times 1}]$ are the point-wise convolution kernel filters. The output $\tilde{C} = [\tilde{C}^1, \tilde{C}^2, \dots, \tilde{C}^{C_E} | \tilde{C}^i \in \mathbb{R}^{H_E \times W_E}]$ is expressed as

$$\tilde{C}^i = T^i \otimes C^i, \quad (5)$$

where \otimes refers to the element-wise multiplication involving C^i (individual feature maps) of the encoder volume \mathbf{C} . Unlike Ref. [25, 26], which employed Global Average Pooling along with an artificial neural network to generate weights, this mechanism uses depth-wise convolutions. It aids independent learning of spatial patterns from each of the activation maps. This is important because each map is a representative of a distinct set of patterns. Besides, with such a fully convolutional module there exists no dependency on the dimensions of the input tensor; thus making the module flexible for incorporation in other architectures.

3.2.2. Spatial attention

The i th spatial attention weight Q^i , illustrated in the upper branch of the *SpaCh* block in Fig. 1, is computed as

$$\mathbf{Q}^i = \Upsilon[\sigma(\sum_{l=1}^{C_E} w_b^k * \zeta^l)], \quad (6)$$

where

$$\zeta^l = \rho\{(\sum_{j=1}^{C_E} w_{SP}^k * S^j) \oplus (\sum_{j=1}^{C_E} w_{SC}^k * \tilde{C}^j)\}, \quad (7)$$

with $\mathbf{W}_{SP} = [w_{SP}^1, w_{SP}^2, \dots, w_{SP}^{C_E} | w_{SP}^i \in \mathbb{R}^{1 \times 1}]$, $\mathbf{W}_{SC} = [w_{SC}^1, w_{SC}^2, \dots, w_{SC}^{C_E} | w_{SC}^i \in \mathbb{R}^{2 \times 2}]$ and $\mathbf{W}_b = [w_b^1, w_b^2, \dots, w_b^{C_E} | w_b^i \in \mathbb{R}^{1 \times 1}]$ being the different convolution filters characterizing the spatial attention mechanism. Here $\rho(x) : \max(0, x)$ and $\sigma(x) : \frac{1}{1+e^{-x}}$ denote the ReLU and sigmoid activation functions, respectively, and Υ represents the up-sampling operation using bilinear interpolation.

The spatially recalibrated output features $\hat{\mathbf{C}} = [\hat{C}^1, \hat{C}^2, \dots, \hat{C}^{C_E} | \hat{C}^i \in \mathbb{R}^{H_E \times W_E}]$ are obtained through an element-wise multiplication \otimes of $\tilde{C}_k \in \mathbb{R}^{C_E}$, with the weight $Q^i \in [0, 1]$ derived from the decoder signal volume \mathbf{S} . We obtain

$$\hat{C}^i = Q^i \otimes \tilde{C}_k. \quad (8)$$

Instead of highlighting the relevant locations in the input encoder signal volume \mathbf{C} with the generated weights $\mathbf{Q} = [Q^1, Q^2, \dots, Q^{C_E}]$ (as in Ref. [25, 26]), our formulation of channel-wise weighted encoder feature map volume $\tilde{\mathbf{C}}$ gets recalibrated by the weights generated through the spatial attention mechanism to produce the refined signal

\hat{C} . This approach helps figure out the relevant channel attention-activated maps initially from the entire volume, followed by focusing within them (through spatial attention) on only those locations carrying important information about the region of interest. This allows saving on the computational resources involved.

3.3. Deep supervision

It is challenging to train deep networks due to problems like the vanishing gradient, which produce an adverse impact on weight updating; particularly, in the earlier layers. This leads to poorer generalisation capability at these layers. Often deep supervision is introduced at the intermediate levels of the network to circumvent the problem [31]. It also aids in the learning of better feature representations for the target region in the feature maps at the hidden layers. Instead of applying deep supervision at the decoder end [32, 26], we propose to apply the mechanism at the encoder end; thereby, enabling the activation maps at the shallower levels of the encoder arm to learn more relevant features of the target region towards improved segmentation. Therefore, we attach additional decoder branches at the second, third and fourth levels of the encoder arm, as illustrated in Fig. 1. These auxiliary decoding paths, attached to the different levels of the encoding path, provide additional supervision during training. Minimization of the loss function $\mathcal{L}_{supervision}$ at the output of the deep supervision module aids in enhancing the quality of the output activation at every level of the encoder. The impact of vanishing gradient is reduced by incorporating the gradients obtained from these auxiliary decoder branches along with the final output layer.

Let $\Theta = [\theta_1, \theta_2]$ consist of $\theta_1 = [W_{11}, W_{21}, W_{22}, W_{31}, \dots, W_{33}, W_{41}]$, representing the weights for the auxiliary deep supervision branches, and $\theta_2 = [W_1, \dots, W_7]$ corresponding to the weights of the encoding path (as illustrated in Fig. 1). The adaptation is expressed as

$$\Theta = \Theta - \eta \frac{\partial \mathcal{L}_{supervision}}{\partial \Theta}, \quad (9)$$

where $\mathcal{L}_{supervision}$ is the auxiliary deep supervision loss and η is the learning rate.

3.4. Loss functions

A significant problem encountered in medical image segmentation arises due to the severe class imbalance, often existing in a target region-of-interest (to be delineated) *vis-a-vis* the background region. This causes the final predictions of the model to be influenced by the dominant non-target (or background) regions. Dice loss [33] (DL) addresses the class imbalance issue between the foreground and background pixels. It is defined as

$$DL = 1 - \left(\frac{2TP + \epsilon}{2TP + FN + FP + \epsilon} \right) = 1 - \left(\frac{2 \sum_{i=1}^N \hat{y}_i y_i + \epsilon}{2 \sum_{i=1}^N \hat{y}_i y_i + \sum_{i=1}^N y_i (1 - \hat{y}_i) + \sum_{i=1}^N (1 - y_i) \hat{y}_i + \epsilon} \right) = 1 - \left(\frac{2 \sum_{i=1}^N \hat{y}_i y_i + \epsilon}{\sum_{i=1}^N \hat{y}_i + y_i + \epsilon} \right), \quad (10)$$

where \hat{y}_i and y_i are the predicted and ground truth value for the i th pixel, respectively, N is the total number of pixels, ϵ is a small random constant, TP , FN , FP correspond to the true positive, false negative, false positive, respectively. However, a significant disadvantage of this loss function is that it does not account for the output imbalance, encompassing FP and FN , in the segmentation output [34], [35]. *Precision* specifies the proportion of pixels correctly identified as belonging to a given class (here, lesion region), relative to the total number of pixels

annotated as representing that actual class. The percentage of correctly identified positive pixels (here, lesion) out of all positive pixels present in the ground truth, is represented by the metric *Recall*.

$$Precision = \frac{TP}{TP + FP}, \quad (11)$$

$$Recall = \frac{TP}{TP + FN}. \quad (12)$$

It is observed that training only with *DL* results in an increased *Precision* at the expense of diminished *Recall*. This is evident from the difference in the scores of *Precision* and *Recall* in Table 3.

The Tversky loss (*TL*) [36] alleviates the problem of *FP* and *FN* by assigning them with weight values α and β , respectively.

$$TL = 1 - \left(\frac{TP + \epsilon}{TP + \alpha FN + \beta FP + \epsilon} \right) = 1 - \frac{\sum_{i=1}^N \hat{y}_i y_i + \epsilon}{\sum_{i=1}^N \hat{y}_i y_i + \alpha \sum_{i=1}^N y_i (1 - \hat{y}_i) + \beta \sum_{i=1}^N (1 - y_i) \hat{y}_i + \epsilon}. \quad (13)$$

An enhanced version of *TL*, called Focal Tversky loss *FTL* [35], involves an additional parameter γ which helps target the imbalanced (smaller) Regions of Interest (ROIs) by exponentially increasing the loss for pixels with low predicted probability. This is expressed as

$$FTL = (TL)^{\frac{1}{\gamma}}. \quad (14)$$

We propose a novel linear combination \mathcal{L} of the loss functions *DL* and *FTL*, for training our *MiADS-Net*; thereby, utilizing the benefits of handling class imbalance while improving upon the balance between *Precision* and *Recall*. Here

$$\mathcal{L} = \sum_l (DL_l + FTL_l), \quad (15)$$

for l classes. Note that $l \in 0, 1$ for binary segmentation. The total loss is computed as

$$\mathcal{L}_{total\ loss} = \mathcal{L}_{supervision} + \mathcal{L}_{output}, \quad (16)$$

where

$$\mathcal{L}_{supervision} = \mathcal{L}_{output} = \mathcal{L}, \quad (17)$$

The values of the hyperparameters α , β , γ , were set at 0.7, 0.3, $\frac{4}{3}$, respectively [35].

3.5. Performance metrics

The *DSC*, *Precision*, *Recall*, *SPE*, and *IoU* are employed to evaluate the segmentation produced by the *MiADS-Net*. The *DSC* is a harmonic mean of *Precision* and *Recall*, and measures the similarity between the predicted mask and the ground truth for a sample CT slice. The *SPE* measures the ability of the model to correctly identify pixels representing the background region (here, healthy lung tissues) out of all the pixels annotated as belonging to the background. Another important metric for the segmentation task is *IoU*, which calculates the amount of overlap between the predicted mask and the available ground truth. All these metrics have values lying in the range [0,1]. They are expressed as

$$DSC = \frac{2TP}{2TP + FP + FN}, \quad (18)$$

$$SPE = \frac{TN}{TN + FP}, \quad (19)$$

$$IoU = \frac{TP}{TP + FP + FN}. \quad (20)$$

Here TN denotes *True Negative*. A classifier is represented in terms of a graphical plot between the *True Positive Rate (TPR)* and *False Positive Rate (FPR)*, at varying thresholds of classification. *Receiver Operating Characteristic (ROC)* curve is used as a comparative measure to evaluate between the classifiers. The Area Under the Curve (AUC) of each model is also a good evaluation measure. The model performance, under various loss functions, is depicted in terms of the Area Under the *Precision-Recall* curve ($AUC-PR$).

4. Experimental Results

Here we outline the data sets used in the study, the implementation details, qualitative and quantitative experimental results, along with their comparative analysis.

4.1. Datasets

Table 2: Datasets used

No.	Name	No. of annotated samples	No. of slices with lesions
1	MOSMED [14]	50	785
2	MedSeg-COV-1 [15]	>40	100
3	MedSeg-COV-2 [16]	9	373
4	COV-CT-Lung-Inf-Seg [17]	10	1351

The COVID-19 lung CT slices were obtained from four publicly available datasets, as tabulated in Table 2. Dataset-1 [14] is a set of lung CT scans taken from 1110 patients belonging to five categories *viz.* CT-0, CT-1, CT-2, CT-3, CT-4. While CT-0 corresponds to the normal cases, the rest of the data is split into four groups according to increased severity of infection in the lung. Here CT-1 has 684 samples with affected lung percentage of 25% or below, CT-2 has 125 samples with affected area ranging from 25% to 50%, CT-3 consisting of 45 samples having 50% to 75% of affected lung region, and CT-4 encompassing just two samples with 75% and above affected lung portion. Only 50 scans, belonging to CT-1, were annotated with binary masks depicting regions of GGO. The affected lung area was assigned a label “1”, and the rest of the slice (unaffected portion without the lesion, as well as the background region) were assigned the label “0”. The CT volumes with annotated masks were used for our study. Dataset-2 [15] consists of 100 axial CT slices from > 40 COVID-positive patients. The slices were labelled by a radiologist to demarcate three different pathologies of COVID-19 *viz.* GGOs, white consolidations and pleural effusion. Dataset-3 [16] encompasses nine volumetric lung CT scans obtained from the Italian Society of Medical Interventional Radiology. However, out of a total of 829 slices, only 373 slices are provided with annotations indicating the regions with GGOs and white consolidations. Dataset-4 [17] is a collection of lung CT scans from 20 patients, with annotations done by two radiologists which were later validated by another experienced radiologist.

The ground truth of these slices consists of only two labels: “1” and “0” to indicate the diseased tissues and other regions (comprising healthy regions of lung and background). Here we used lung CT volumes from the first ten patients for extracting the slices in our experiments. This was because the remaining 10 samples contained non-uniform number of slices, being indicative of dissimilarity in the voxel spacing.

All the slices were resized to a dimension of 512×512 . The voxel intensities of all CT volumes, from the four data sources, were clipped to make them lie in the range [1000 HU, 170 HU], in order to filter out unnecessary details and noise. This was followed by intensity normalisation across the resultant multi-source database. Since all the CT slices in the volume do not contain COVID lesions, we selected only those having embedded lesions for the training. To account for the fact that not all datasets included labels for every possible COVID-19 pathology, we combined these different pathologies from Datasets 2 and 3 to create a single class representing COVID-19 lesions. The extracted slices from the four multi-source datasets were combined into a single database, to yield a total of 2609 annotated slices. This combined dataset was next randomly divided into five parts, for five-fold cross validation. Pooling the extracted multi-source slices into one single dataset helped the model attain better generalization to learn the varying COVID-19 lesion structures and appearance (corresponding to different severity levels). We also utilized the additional ten patient lung masks from Dataset-4 to train the model for segmenting the lung region in the input CT slice while evaluating the severity of infection.

4.2. Results

The experimental setup for *MiADS-Net* was implemented in Python 3.9 on a 12GB NVIDIA GeForce RTX 2080 Ti GPU. Optimizer Adam was used with an initial learning rate of 0.0001 for the first 35 epochs; which was subsequently reduced to 0.00001 for the remaining 65 epochs. Learning rate was reduced by a factor of 50%, when there was no further improvement in loss value after five consecutive epochs. Early stopping was employed to prevent overfitting. Both qualitative and quantitative analysis was made to evaluate the segmentation performance of the proposed *MiADS-Net*. Comparative study with related state-of-the-art deep segmentation architectures demonstrate the superiority of our model, under different ablation experiments. The severity of infection was also estimated.

Table 3: Effect of loss functions on the performance metrics

Loss functions	DSC	IoU	Precision	Recall
Focal Tversky Loss	0.8146	0.6964	0.7994	0.8386
Dice Loss	0.8217	0.7042	0.8593	0.7945
Focal Tversky Loss + Dice Loss	0.8293	0.7159	0.8372	0.8241
Focal Loss + Dice Loss	0.8192	0.70	0.8706	0.7799

4.2.1. Ablations

The effect of loss functions, *viz.* FTL , DL , $FL+DL$, $FTL+DL$, was investigated on the performance metrics of eqns. (11), (12), (18), (20), using the combined annotated dataset (as elaborated above). This is presented in Table 3. It is observed that DSC and IoU were the highest, when the proposed combined loss function of eqn. (15) was

used [Row 3 in the table]. The number of pixels corresponding to infected lung region(s) is found to be significantly lower than the number of pixels from the background region, thereby resulting in major class imbalance.

Fig. 3 corroborates that $AUC-PR$ is the highest for the proposed combination, signifying the correct classification of a majority of the pixels. Even in scenarios involving smaller ROIs, it can achieve a better balance between *Precision* and *Recall*.

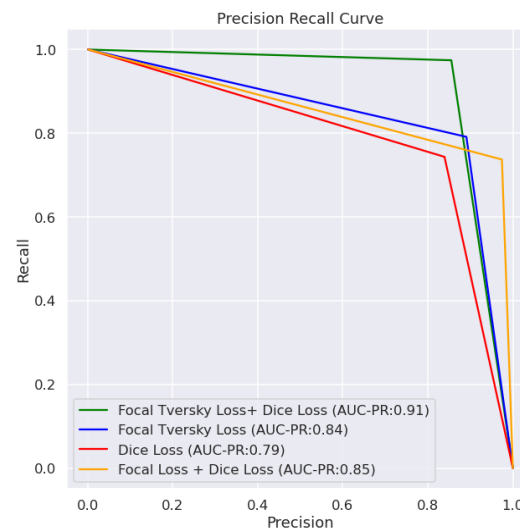


Figure 3: *Precision-Recall* curves for the different loss functions using the combined annotated dataset

Table 4: Effect of different modules in *MiADS-Net* using the combined annotated dataset

Approach	<i>DSC</i>	<i>Precision</i>	<i>Recall</i>	<i>SPE</i>	<i>IoU</i>
<i>U-Net</i> backbone + Supervision + <i>SpaCh</i> with <i>AsDiC</i>	0.8145±0.014	0.8143±0.013	0.8216±0.0205	0.9976±0.0007	0.6962±0.0201
<i>U-Net</i> backbone + Supervision + <i>SpaCh</i> w/o <i>AsDiC</i>	0.8006±0.019	0.7984±0.025	0.8193±0.018	0.9975±0.0003	0.6787±0.026
<i>U-Net</i> backbone + <i>SpaCh</i> with <i>AsDiC</i>	0.7698±0.033	0.7711±0.032	0.7909±0.0303	0.9971±0.0004	0.6408±0.0419
<i>U-Net</i> backbone + <i>SpaCh</i> w/o <i>AsDiC</i>	0.7356±0.023	0.7631±0.084	0.7553±0.066	0.997±0.0009	0.5983±0.03
<i>U-Net</i> backbone + Supervision only	0.7839±0.009	0.7941±0.022	0.7982±0.029	0.9976±0.0004	0.6594±0.0107
Vanilla <i>U-Net</i>	0.6306 ± 0.067	0.7821 ± 0.072	0.5916 ± 0.068	0.9969 ± 0.001	0.4873 ± 0.712

Next some experiments were conducted to validate the role of *SpaCh* and *AsDiC* blocks on the performance of the vanilla *U-Net* using the combined annotated dataset. It is observed from Table 4 that addition of just the *SpaCh* block led to a rise in *DSC*. Upgrading the *SpaCh* block with the *AsDiC* module resulted in a significant increase in the *Recall* score; implying a decrease in *FN* pixels. To better understand the impact of the proposed mixed attention mechanism, we present in Fig. 4 a few sample feature maps at the input and output of the *SpaCh* block. It is evident that regions corresponding to the infected lung tissues get prominently displayed within the output feature maps (highlighted by yellow circles) in column (d) of the figure after passing through the *SpaCh* module.

The incorporation of *deep supervision* to the basic *U-Net* framework resulted in an increment by a margin of >10 % in the *DSC* and *IoU*. A significant rise in both *Precision* and *Recall* are indicative of a simultaneous decrease in *FN*. Inclusion of *deep supervision*, in conjunction with *SpaCh* block, further enhanced the performance of *MiADS-Net*; with precise segmentation, as expressed by highest *DSC* and *Recall* scores in Row 1 of Table 4.

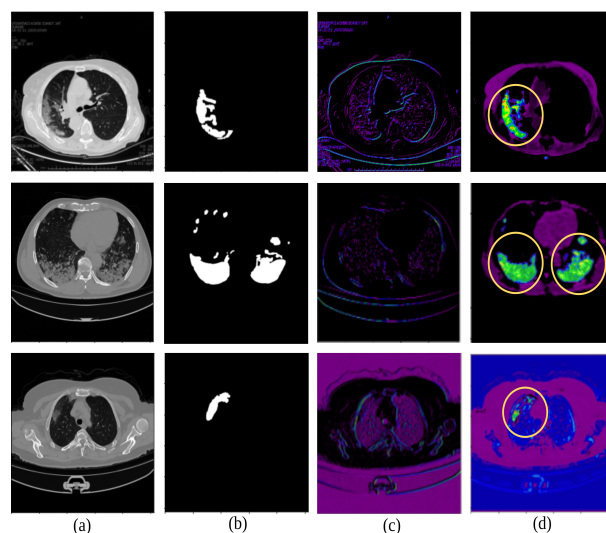


Figure 4: Impact of *SpaCh* block, visualized with reference to (a) sample input CT slices, (b) corresponding ground truth, and the feature maps of *SpaCh* block as displayed at its (c) input, & (d) output.

Fig. 5 presents a visualization of the decrease in pixel count of *FN* pixels with respect to the segmentation output generated by the vanilla *U-Net*, as the different modules are added in the *MiADS-Net*. It is observed that by incorporating both spatial and channel attention mechanisms (in terms of *SpaCh* and *AsDiC* modules), a better segmentation is obtained (both qualitatively and quantitatively) with reference to the ground truth. Adding deep supervision generated the best outcome, as evident from part (f) of the figure.

Inclusion of deep supervision (at the encoder arm) generated feature map volumes containing activation maps which focused on relevant patterns and features in the ROI, as observed from Fig. 6. The marked areas within the circles of part (d) of the figure are found to represent the extracted features corresponding to the anatomy of the lesions (with reference to the ground truth).

4.2.2. Comparisons

Table 5: Comparative study, over performance metrics, with related state-of-the-art architecture

Models	<i>DSC</i>	<i>Precision</i>	<i>Recall</i>	<i>SPE</i>	<i>IoU</i>
<i>MiADS-Net</i>	0.8145±0.014	0.8143±0.013	0.8216±0.0205	0.9976±0.0007	0.6962±0.0201
Attention <i>U-Net</i> [9]	0.6587 ± 0.043	0.7537 ± 0.0751	0.6445 ± 0.038	0.9946 ± 0.006	0.52156 ± 0.041
<i>U-Net</i> [8]	0.6306 ± 0.067	0.7821 ± 0.072	0.5916 ± 0.068	0.9969 ± 0.001	0.4873 ± 0.712
<i>U-Net++</i> [10]	0.6881 ± 0.039	0.7209 ± 0.038	0.7083 ± 0.048	0.9961 ± 0.001	0.5456 ± 0.039
Residual <i>U-Net</i> [11]	0.6501 ± 0.018	0.7837 ± 0.047	0.6004 ± 0.044	0.9980 ± 0.0006	0.5123 ± 0.017

Table 5 presents a comparative study of *MiADS-Net* with state-of-the-art models, like *U-Net*, *U-Net++*, *Attention U-Net* and *Residual U-Net*, employing five-fold cross validation over the various performance metrics *DSC*, *Recall*, *IoU*, *Precision* and *SPE* (based on the combined annotated dataset). The best scores are marked in bold in the table. It is evident that *MiADS-Net* outperforms the remaining models.

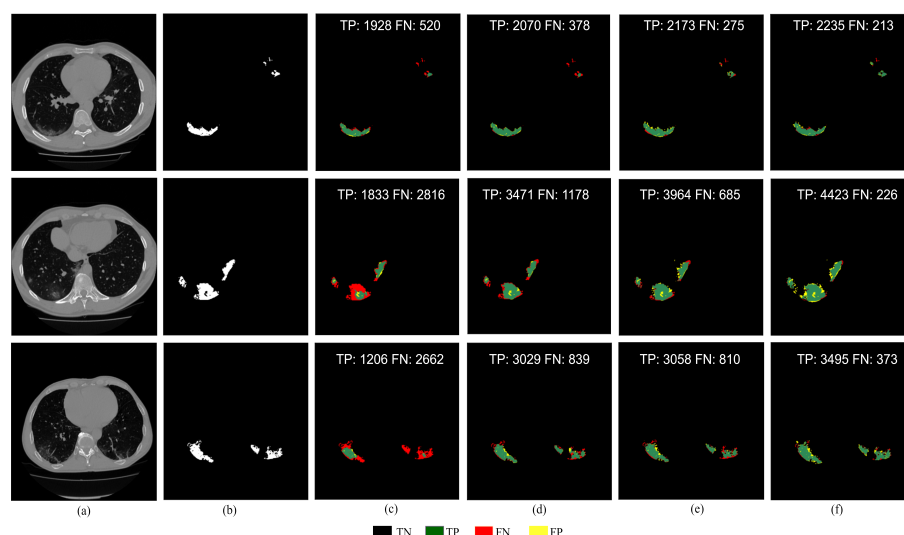


Figure 5: Segmentation on sample patients, using combined annotated dataset, depicting (a) input CT slice having (b) ground truth mask of lesions, and corresponding output generated by (c) vanilla *U-Net*, with incorporation of (d) *SpaCh* module *w/o AsDiC*, (e) *SpaCh* module *with AsDiC*, (f) additional deep supervision.

This reiterates the contention that by extending the vanilla *U-Net* framework with the novel mixed attention modules of *SpaCh* and *AsDiC*, along with the *deep supervision* mechanism, enables *MiADS-Net* to accurately identify the pixels belonging to the COVID-19 lesion category with a smaller number of *FN*s. By focusing only on the significant features that correspond to the target lesion regions, our architecture is found to be more effective in separating the target region(s) from a CT slice.

The values of *DSC* and *IoU*, the most widely used metrics of evaluation in medical image segmentation, demonstrate discernible improvement; thereby, establishing the efficacy of *MiADS-Net*. Significant improvement in both *Precision* and *Recall* metrics indicate greater detection of *TP* pixels, with simultaneous reduction in the *FP*s. This validates the effectiveness of *MiADS-Net* in capturing the structure of the infection lesions encompassing blurred edges with irregular contours and shapes.

Results are corroborated in terms of corresponding confusion matrices in Fig. 7. The box plot of *DSC* and the *ROC* curve with *AUC* in Fig. 8 additionally emphasize the superiority of our *MiADS-Net*.

Fig. 9 displays a qualitative study of the segmentation maps (on six sample CT scans), generated by our *MiADS-Net*, and compared with respect to the related state-of-the-art models (referred above). It is evident that the vanilla *U-Net*, Attention *U-Net*, Residual *U-Net*, and *U-Net++* are unable to extract the entire lesion region appropriately. Presence of *FN* pixels can be clearly viewed in the corresponding maps. On the other hand, the segmentation map of the *MiADS-Net* indicates the highest concentration of *TP* pixels. It is visually evident that the *MiADS-Net* outperforms the compared baseline architectures by more accurately segmenting the affected lung tissue, as observed from the sample CT slices.

Finally a comparative tabulation of a few other related state-of-the-art models (from literature), dealing with delineation of COVID lesions from lung CT, is provided in Table 6 in terms of *DSC*. The superiority of our *MiADS-Net* is apparent.

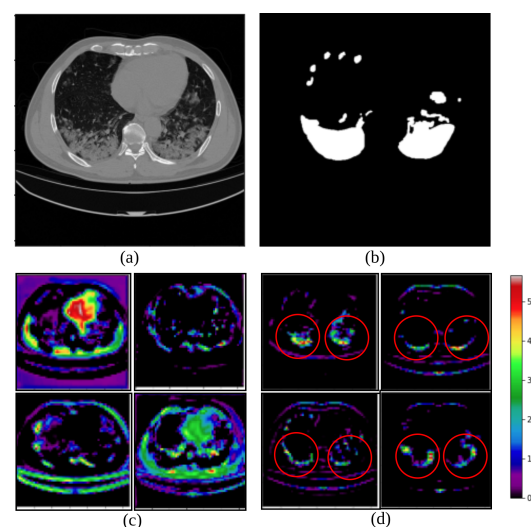


Figure 6: Feature maps from the fourth level of the encoder branch, using the combined annotated dataset. Sample (a) input CT slice, with (b) ground truth, and corresponding feature maps set (c) *without* deep supervision, and (d) with auxiliary *deep supervision*.

4.2.3. Severity of infection

The severity grading of a sample patient was computed, based on the infection region in the corresponding lung CT. The predicted lung mask and the lesion segmentation mask were used to calculate the ratio of the affected lung area to total lung area, individually for the left and right lung. The maximum of these two ratios determined the grade of severity of infection in the patient [2]. The severity grades are assigned according the following criteria:

- CT-0: Healthy patients
- CT-1: Patients with infected lung % <25
- CT-2: Patients with infected lung % between 25-50
- CT-3: Patients with infected lung % between 50 and 75
- CT-4: Patients with infected lung % >75

Fig. 10 depicts the sample lung CT slices of five different patients, highlighting their maximum visible lung area with reference to the total CT volume in each case. The ratio computation results in the following prediction.

- Patient-1: Affected Left Lung % = 81.92, Affected Right Lung % = 69.00, Grade: CT-4;
- Patient-2: Affected Left Lung % = 7.75, Affected Right Lung % = 2.27, Grade: CT-1;
- Patient-3: Affected Left Lung % = 31.00, Affected Right Lung % = 23.06, Grade: CT-2;
- Patient-4: Affected Left Lung % = 38.36, Affected Right Lung % = 6.40, Grade: CT-2;
- Patient-5: Affected Left Lung % = Nil, Affected Right Lung % = Nil, Grade: CT-0.

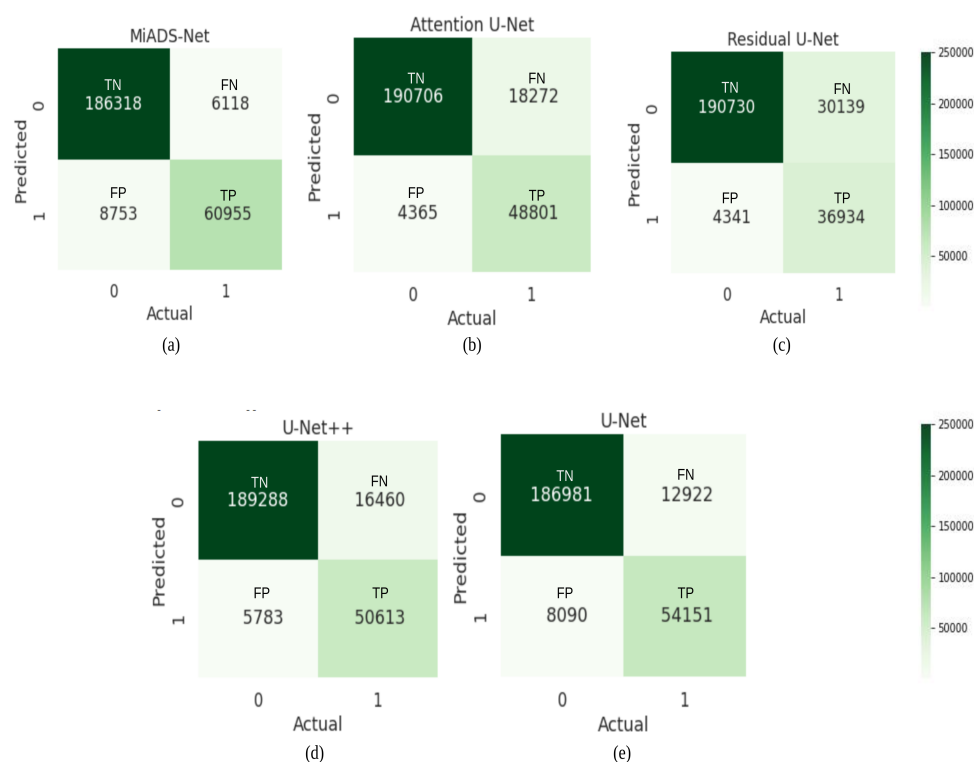


Figure 7: Confusion matrix, with combined annotated dataset, generated by (a) *MiADS-Net*, (b) Attention *U-Net*, (c) Residual *U-Net*, (d) *U-Net++*, and (e) vanilla *U-Net*.

5. Conclusions and Discussion

A novel deep architecture *MiADS-Net*, incorporating mixed attention and deep supervision, has been developed for the accurate segmentation of COVID lesions from lung CT slices. The *SpaCh* and *AsDiC* modules contribute towards mixed attention for effective delineation of irregular shapes and contours of lesions, their low contrast, and associated blurring. The network allows highlighting important activation maps, while focusing on key locations within them; thereby, allowing *MiADS-Net* to accurately delineate the relevant lesions. Deep supervision enables learning of stronger and more discriminating features at shallower levels of the network. This enhances the output segmentation quality. Class imbalance and false negatives are tackled using a linear combination of Dice loss and Focal Tversky loss, while outlining the lesion structure. This also leads to accurate computation of the affected lung area to help grade the severity of infection.

In the absence of sufficient annotated samples, the model could not be trained to distinguish between the different pathologies, like GGO, white consolidation, and pleural effusion. The research is currently being extended to multi-class segmentation. It can result in an effective tool for the screening and early detection of patients who may have contracted the COVID-19 pathogen. In individual patients infected with the virus, and demonstrating associated pulmonary abnormalities, the same methodologies can be used to accurately and more rapidly assess disease progression and guide therapy with effective patient management. Volumetric modeling of the lung can help in determining the optimal prognostics for recovery, based on the existing damage. Incorporation of additional genomic inputs is expected to throw further illumination on the investigation.

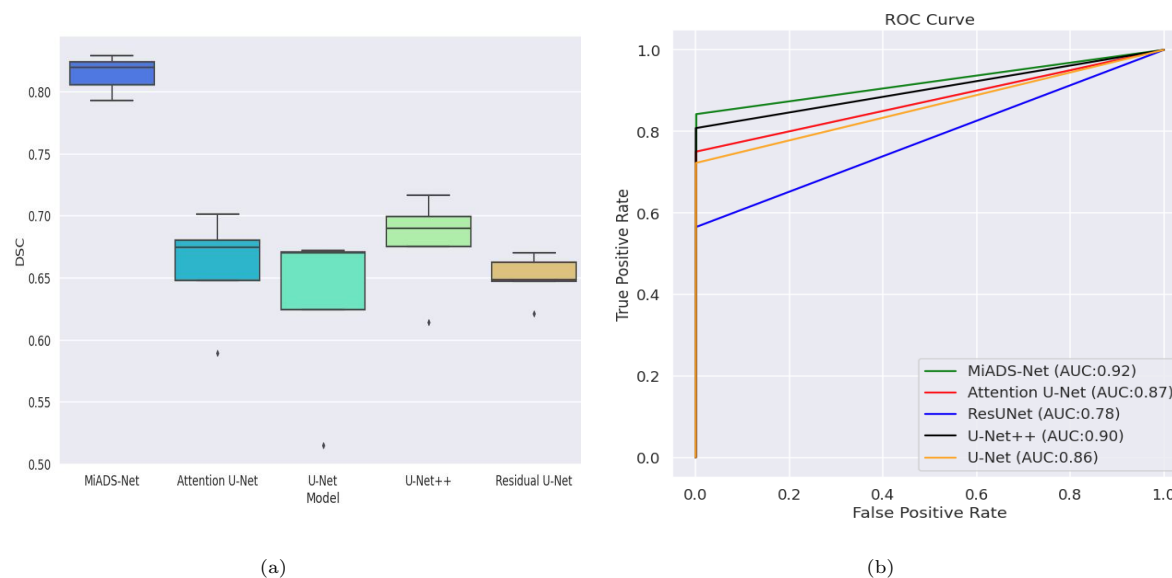


Figure 8: Comparative study with related models, on the combined annotated dataset, using (a) Box plot in terms of DSC , and (b) ROC curves with AUC .

References

- [1] O. Gozes, M. Frid-Adar, and *et al.*, “Rapid AI development cycle for the Coronavirus (COVID-19) pandemic: Initial results for automated detection & patient monitoring using deep learning CT image analysis,” *arXiv:2003.05037*, 2020. [Online]. Available: <https://spectrum.ieee.org/hospitals-deploy-ai-tools-detect-covid19-chest-scans>
- [2] S. P. Morozov, V. Y. Chernina, A. I. Blokhin, and V. A. Gomboleviskiy, “Chest computed tomography for outcome prediction in laboratory-confirmed COVID-19: A retrospective analysis of 38,051 cases,” *Digital Diagnostics*, vol. 1, no. 1, pp. 27–36, 2020.
- [3] Y. LeCun, Y. Bengio, and G. Hinton, “Deep learning,” *Nature*, vol. 521, pp. 436–444, 2015.
- [4] K. He, X. Zhang, and *et al.*, “Deep residual learning for image recognition,” in *Proceedings of the IEEE Conference on Computer Vision and Pattern Recognition*, 2016, pp. 770–778.
- [5] S. H. Gao, M. M. Cheng, and *et al.*, “Res2Net: A new multi-scale backbone architecture,” *IEEE Transactions on Pattern Analysis and Machine Intelligence*, vol. 43, pp. 652–662, 2019.
- [6] G. Huang, Z. Liu, and *et al.*, “Densely connected convolutional networks,” in *Proceedings of the IEEE Conference on Computer Vision and Pattern Recognition*, 2017, pp. 4700–4708.
- [7] V. Badrinarayanan, A. Kendall, and *et al.*, “SegNet: A deep convolutional encoder-decoder architecture for image segmentation,” *IEEE Transactions on Pattern Analysis and Machine Intelligence*, vol. 39, pp. 2481–2495, 2017.

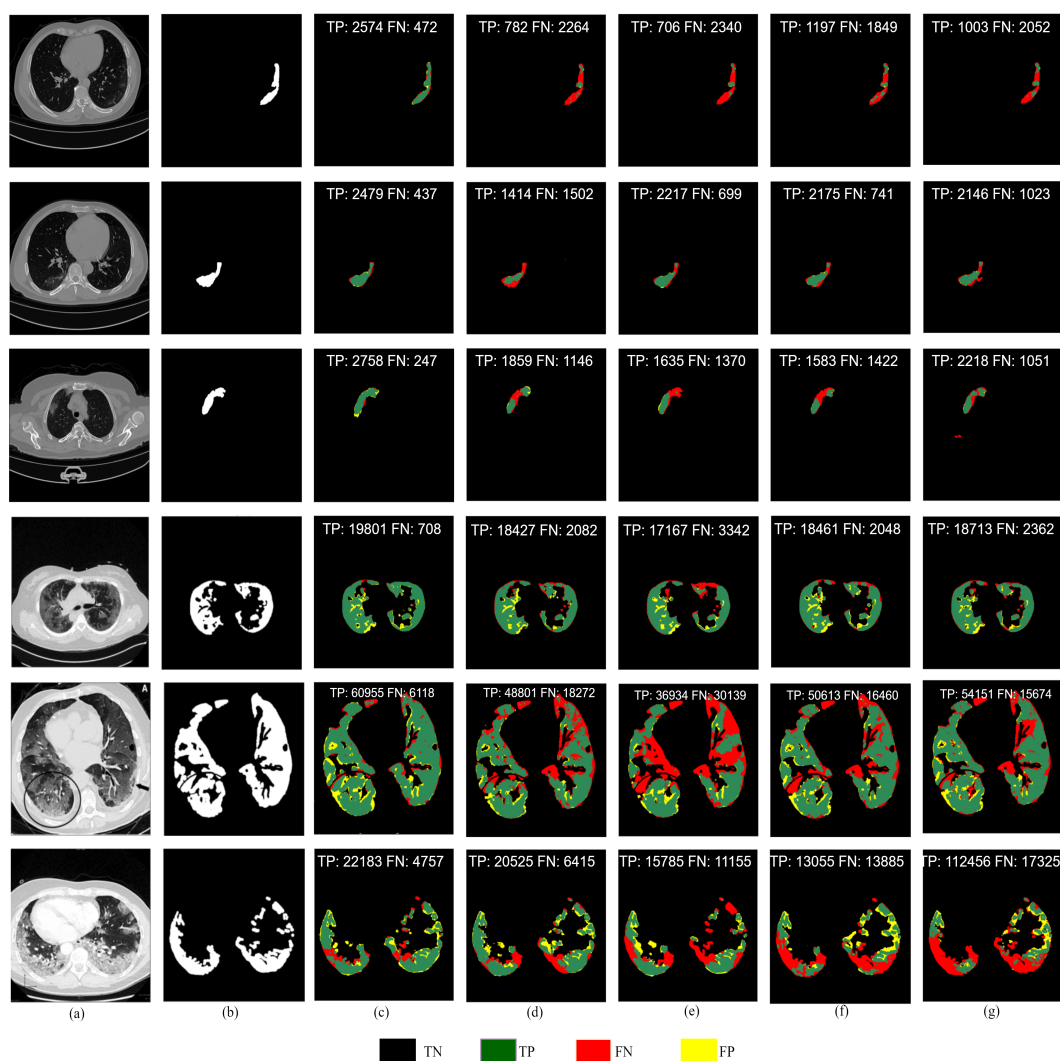


Figure 9: Qualitative comparison in segmentation output of *MiADS-Net* with related state-of-the-art deep learning architectures, using the combined annotated dataset. (a) Sample CT slice, (b) the corresponding ground truth of the lesion, with predicted segmentation by (c) *MiADS-Net*, (d) Attention *U-Net* (e) *U-Net*, (f) *U-Net++*, and (g) Residual *U-Net*.

- [8] O. Ronneberger, P. Fischer, and *et al.*, “*U-Net*: Convolutional networks for biomedical image segmentation,” in *Proceedings of the International Conference on Medical Image Computing and Computer Assisted Intervention, (MICCAI)*. Springer, 2015, pp. 234-241.
- [9] O. Oktay, J. Schlemper, and *et al.*, “Attention *U-Net*: Learning where to look for the pancreas,” in *Proceedings of the Medical Imaging with Deep Learning*, 2018.
- [10] Z. Zhou, R. Siddiquee, and *et al.*, “*UNet++*: A nested *U-Net* architecture for medical image segmentation,” in *Deep Learning in Medical Image Analysis and Multimodal Learning for Clinical Decision Support*. Springer, 2018, pp. 3-11.
- [11] A. Khanna, N. D. Londhe, and *et al.*, “A deep Residual *U-Net* convolutional neural network for automated lung segmentation in computed tomography images,” *Biocybernetics and Biomedical Engineering*, vol. 40, no. 3, pp. 1314-1327, 2020.

Table 6: Comparative study with recent literature, in segmenting COVID lesions from lung CT

Model	Characteristics	Dataset		DSC
		Train Set	Test Set	
MiADS-Net	Channel & spatial attention, with deep supervision	80% of CT images from MOSMED [14], MedSeg-COV-1 [15], MedSeg-COV-2 [16] and COV-CT-Lung-Inf-Seg [17]	20% of CT images from MOSMED [14], MedSeg-COV-1 [15], MedSeg-COV-2 [16] and COV-CT-Lung-Inf-Seg [17]	0.82
Inf-Net	Parallel partial decoder to generate coarse output, with refinement by reverse reverse and edge attention	45 randomly selected CT images from MedSeg-COV-1 [15]	50 CT images from MedSeg-COV-1 [15],	0.682
Goncharov et al	Multi-task approach for segmentation with classification	MOSMED [14], MedSeg-COV-2 [16], COV-CT-Lung-Inf-Seg [17]	MOSMED [14]	0.63
D2A-Net	Dual-attention and hybrid dilated convolutions	MedSeg-COV-2 [16], COV-CT-Lung-Inf-Seg [17]	MedSeg-COV-1 [15]	0.72
nCoVSegNet	Transfer learning, channel and spatial attention	40 cases from MOSMED [14], LIDC-IDRI	10 cases from MOSMED [14], COV-CT-Lung-Inf-Seg [17]	0.69
LCOV-Net	Lightweight CNN with attention	80% of CT images from 10 private hospitals	20% of CT images from 10 private hospitals	0.78

- [12] V. S. Tseng, J. J. C. Ying, and *et al.*, “Computational intelligence techniques for combating COVID-19: A survey,” *IEEE Computational Intelligence Magazine*, vol. 15, pp. 10-22, 2020.
- [13] J. S. Suri, S. Agarwal, and *et al.*, “A narrative review on characterization of acute respiratory distress syndrome in COVID-19-infected lungs using artificial intelligence,” *Computers in Biology and Medicine*, vol. 130, p. 104210, 2021. [Online]. Available: <https://doi.org/10.1016/j.compbiomed.2021.104210>
- [14] S. P. Morozov, A. E. Andreychenko, and *et al.*, “MOSMED data: Data set of 1110 chest CT scans performed during the COVID-19 epidemic,” *Digital Diagnostics*, vol. 1, pp. 49-59, 2020.
- [15] MedSeg, H. B. Jenssen, and T. Sakinis, “MedSeg Covid Dataset 1,” 1 2021. [Online]. Available: https://figshare.com/articles/dataset/MedSeg_Covid_Dataset_1/13521488
- [16] “COVID-19 CT Segmentation Dataset,” 2020. [Online]. Available: <http://medicalsegmentation.com/covid19/>
- [17] J. Ma, C. Ge, and *et al.*, “COVID-19 CT Lung and Infection Segmentation Dataset,” Apr. 2020. [Online]. Available: <https://doi.org/10.5281/zenodo.3757476>
- [18] L. Li, L. Qin, and *et al.*, “Artificial intelligence distinguishes COVID-19 from community acquired pneumonia on chest CT,” *Radiology*, vol. 296, 2020. [Online]. Available: <https://doi.org/10.1148/radiol.2020200905>

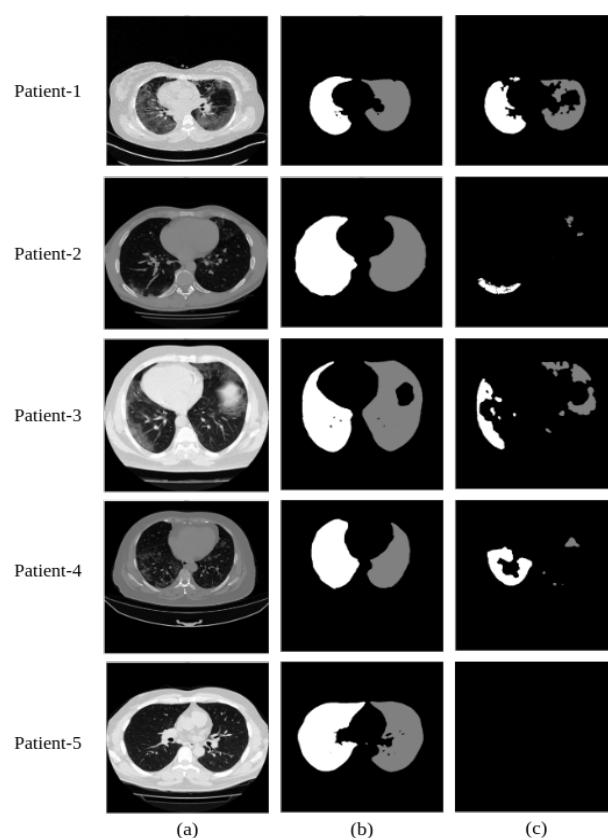


Figure 10: Gradation of severity in sample COVID-infected patients, depicting the (a) lung CT slice, (b) lung mask (white and gray indicating left and right lung, respectively), and the corresponding delineated lesion regions from both lungs.

- [19] S. A. Harmon, T. H. Sanford, and *et al.*, “Artificial intelligence for the detection of COVID-19 pneumonia on chest CT using multinational datasets,” *Nature Communications*, vol. 11, 2020. [Online]. Available: <https://doi.org/10.1038/s41467-020-17971-2>
- [20] Y. H. Wu, S. H. Gao, and *et al.*, “JCS: An explainable COVID-19 diagnosis system by joint classification and segmentation,” *IEEE Transactions on Image Processing*, vol. 30, pp. 3113-3126, 2021. [Online]. Available: <https://doi.org/10.1109/TIP.2021.3058783>
- [21] Z. Han, B. Wei, and *et al.*, “Accurate screening of COVID-19 using attention-based deep 3D multiple instance learning,” *IEEE Transactions on Medical Imaging*, vol. 39, pp. 2584-2594, 2020.
- [22] A. Saood and I. Hatem, “COVID-19 lung CT image segmentation using deep learning methods: *U-Net* versus *SegNet*,” *BMC Medical Imaging*, vol. 21, pp. 1-10, 2021.
- [23] M. Goncharov, M. Pisov, and *et al.*, “CT-Based COVID-19 triage: Deep multitask learning improves joint identification and severity quantification,” *Medical Image Analysis*, vol. 71, p. 102054, 2021. [Online]. Available: <https://doi.org/10.1016/j.media.2021.102054>
- [24] F. Xie, Z. Huang, and *et al.*, “DUDA-Net: A double U-shaped dilated attention network for automatic infection

- area segmentation in COVID-19 lung CT images,” *International Journal of Computer Assisted Radiology and Surgery*, vol. 16, pp. 1425-1434, 2021.
- [25] X. Zhao, P. Zhang, and *et al.*, “D2A U-Net: Automatic segmentation of COVID-19 CT slices based on dual attention and hybrid dilated convolution,” *Computers in Biology and Medicine*, vol. 135, p. 104526, 2021. [Online]. Available: <https://doi.org/10.1016/j.compbiomed.2021.104526>
- [26] T. Zhou, S. Canu, and *et al.*, “Automatic COVID-19 CT segmentation using U-Net integrated spatial and channel attention mechanism,” *International Journal of Imaging Systems and Technology*, vol. 31, pp. 16-27, 2021. [Online]. Available: <https://doi.org/10.1002/ima.22527>
- [27] J. Liu, B. Dong, and *et al.*, “COVID-19 lung infection segmentation with a novel two-stage cross-domain transfer learning framework,” *Medical Image Analysis*, vol. 74, p. 102205, 2021.
- [28] J. Deng, W. Dong, and *et. al.*, “ImageNet: A large-scale hierarchical image database,” in *Proceedings of IEEE Conference on Computer Vision and Pattern Recognition*, 2009, pp. 248-255.
- [29] D. P. Fan, T. Zhou, and *et al.*, “Inf-Net: Automatic COVID-19 lung infection segmentation from CT images,” *IEEE Transactions on Medical Imaging*, vol. 39, pp. 2626-2637, 2020.
- [30] Q. Zhao, H. Wang, and *et al.*, “LCOV-NET: A lightweight neural network for COVID-19 pneumonia lesion segmentation from 3D CT images,” in *Proceedings of the IEEE 18th International Symposium on Biomedical Imaging (ISBI)*, 2021, pp. 42-45.
- [31] C.-Y. Lee, S. Xie, and *et al.*, “Deeply-supervised nets,” in *Artificial Intelligence and Statistics*. PMLR, 2015, pp. 562-570.
- [32] H. Huang, L. Lin, and *et al.*, “UNet 3+: A full-scale connected U-Net for medical image segmentation,” in *Proceedings of the IEEE International Conference on Acoustics, Speech and Signal Processing (ICASSP)*, 2020, pp. 1055-1059.
- [33] F. Milletari, N. Navab, and *et al.*, “V-net: Fully convolutional neural networks for volumetric medical image segmentation,” in *Proceedings of Fourth International Conference on 3D vision (3DV)*. IEEE, 2016, pp. 565-571.
- [34] S. A. Taghanaki, Y. Zheng, and *et al.*, “Combo loss: Handling input and output imbalance in multi-organ segmentation,” *Computerized Medical Imaging and Graphics*, vol. 75, pp. 24-33, 2019.
- [35] N. Abraham and N. M. Khan, “A novel focal Tversky loss function with improved attention U-Net for lesion segmentation,” in *Proceedings of IEEE 16th International Symposium on Biomedical Imaging (ISBI 2019)*, 2019, pp. 683-687.
- [36] S. S. M. Salehi, D. Erdogmus, and *et al.*, “Tversky loss function for image segmentation using 3D fully convolutional deep networks,” in *Proceedings of International Workshop on Machine Learning in Medical Imaging*. Springer, 2017, pp. 379-387.